

## Three-dimensional positron-electron momentum distribution in single-crystal graphite

Ikuzo Kanazawa

*Department of Physics, Tokyo Gakuji University, Koganeishi, Tokyo 184, Japan*

Shoichiro Tanigawa and Ryoichi Suzuki\*

*Institute of Material Science, University of Tsukuba, Tsukuba 305, Japan*

Mizuka Sano

*Department of Chemistry, Faculty of Science, Kumamoto University, Kurokami, Kumamoto 860, Japan*

Hiroo Inokuchi

*Institute for Molecular Science, Okazaki 444, Japan*

(Received 17 August 1989; revised manuscript received 22 June 1990)

The three-dimensional positron-electron momentum distribution in single-crystal graphite is determined from the reconstruction of the measured two-dimensional angular correlation of positron annihilation. The Lock-Crisp-West rate obtained through periodic superposition of the experimentally determined momentum density is compared with the theoretical rate calculated on the basis of linear combination of atomic orbitals  $X\alpha$  by Saito *et al.*

### I. INTRODUCTION

The angular correlation of positron annihilation radiation is one of the methods that directly measure the real momentum distribution of electrons in a crystal.<sup>1</sup> In a previous paper, we presented a two-dimensional angular correlation of annihilation radiation (2D-ACAR) in single-crystal graphite measured along two crystal axes.<sup>2</sup> In order to obtain more information on the electronic structure of graphite, we have extended our study to a three-dimensional momentum distribution by measuring 2D-ACAR in five directions in a graphite crystal and converting the momentum distribution to a distribution in the reduced Bloch wave vector by superposing angular distributions periodically on the basis of the Lock-Crisp-West theorem.<sup>3</sup> The result is compared with the theoretical prediction presented by Saito *et al.*<sup>4</sup>

A 2D-ACAR spectrum,  $N(p_y, p_z)$ , is the projection of momentum density  $\rho(p)$  of two annihilation quanta onto the  $(p_y, p_z)$  plane, and is expressed by

$$N(p_y, p_z) = \int \rho(p) dp_x, \quad (1)$$

where  $p$  is electron-positron pair momentum.<sup>5</sup> The  $x$  direction is taken as a line joining the graphite crystal and the detector of annihilation radiation. In a previous study,<sup>2</sup> the  $x$  direction was taken as a line parallel to the  $[2\bar{1}\bar{1}0]$  or  $[10\bar{1}0]$  axes of the graphite crystal, so that momentum densities projected onto the  $(p[01\bar{1}0], p[0001])$  and the  $(p[\bar{1}2\bar{1}0], p[0001])$  planes were obtained. In this study, positron annihilation radiation has been detected not only in the directions  $[2\bar{1}\bar{1}0]$  and  $[10\bar{1}0]$ , but also in three directions between these two axes, by changing the orientation of the crystal around the  $[0001]$  axis. From these sets of 2D-ACAR measurements, we obtain the three-dimensional positron-electron

momentum density through reconstruction.<sup>6</sup> The reconstruction was performed as follows. Each 2D-ACAR spectrum observed gives two-dimensional autocorrelation,  $B(r)_{2D}$ , through the two-dimensional Fourier transformation

$$B(r)_{2D} = (2\pi)^{-1} \int N(p_y, p_z) \exp[i(p_y + p_z)r] dp_y dp_z. \quad (2)$$

$B(r)_{2D}$  then gives three-dimensional autocorrelation,  $B(r)_{3D}$ , through three-dimensional interpolation, since each  $B(r)_{2D}$  contains the cross section of  $B(r)_{3D}$  at a given point. Fourier transformation of  $B(r)_{3D}$  then provides the three-dimensional momentum density  $D(p)$ . Through these procedures, we have obtained information on the three-dimensional electron momentum distribution in graphite.

According to the Lock-Crisp-West (LCW) theorem,<sup>3</sup> the once-integrated intensity of the positron-annihilation radiation with the electron momentum  $p$  (LCW rate) is defined by

$$\begin{aligned} N(p) &= \sum_G D(p+G) \\ &= c \sum_{b,k} \delta(p-k) \int_{\text{cell}} dr |\psi_{b,k}(r)|^2 |\phi(r)|^2, \end{aligned} \quad (3)$$

where  $\psi_{b,k}(r)$  and  $\phi(r)$  are the Bloch wave functions of the electron and the positron, respectively, and  $G$  is the reciprocal-lattice vector. The summation extends over the occupied band  $b$  and the crystal momentum  $k$ . The integral in  $r$  is taken over a unit cell.

### II. EXPERIMENT

The experimental apparatus is the same as that described in the previous paper.<sup>2</sup> A synthesized Kish-graphite crystal,  $\sim 4 \times 4 \times 0.2$  mm<sup>3</sup>, which was known to

be a fairly good single crystal from its Laue x-ray diffraction pattern, was used for measurements. Four pieces of this crystal with (0001) face orientation were stacked on a carbon-rod support in such a way that their  $[2\bar{1}\bar{1}0]$  axes were all aligned in the same direction, as shown by their Laue diffraction patterns. 2D-ACAR from the piled graphite crystals was observed in five directions:  $0^\circ$ ,  $7.5^\circ$ ,  $15^\circ$ ,  $22.5^\circ$ , and  $30^\circ$  to the  $[2\bar{1}\bar{1}0]$  axis within the plane of (0001). The first direction is parallel to the  $[2\bar{1}\bar{1}0]$  axis and the last parallel to the  $[10\bar{1}0]$  axis. A three-dimensional momentum distribution was reconstructed from these five sets of 2D-ACAR spectra through autocorrelation. In order to justify this reconstruction method, we compared a 2D-ACAR spectrum derived from a reconstructed three-dimensional momentum distribution with an experimentally observed 2D-ACAR spectrum. The 2D-ACAR spectrum was observed for single crystals of hexagonal metals, Ru and Ti, with (0001) and (1100) face orientations.<sup>7</sup> From five sets of 2D-ACAR data for the (0001) orientation, a three-dimensional momentum distribution was reconstructed by the method described above. The three-dimensional momentum distribution was then projected onto the  $(p[1100], p[1000])$  plane. The 2D-ACAR spectrum thus obtained was compared with the 2D-ACAR spectrum directly measured for the other face orientation, i.e., the (1100) orientation. They were found to be in fairly good agreement, the difference between them being less than 2%.

### III. RESULTS AND DISCUSSIONS

Figure 1 shows the first Brillouin zone of graphite and Fig. 2 shows contour maps of momentum density through four cross sections (I–IV) of the three-dimensional positron-electron momentum distribution, reconstructed from 2D-ACAR data. The 2D-ACAR data were collected with the aid of a cross-correlated matching which had two detectors, placed 8 m from the graphite sample. The ordinate and abscissa in Fig. 2 are expressed in terms of the polar and azimuthal angles of one detector as observed from the sample relative to a baseline joining the other detector and the sample. Figure 3 shows a spectrum of annihilation counts integrated along the  $p[01\bar{1}0]$  of the 2D-ACAR spectrum for the  $(2\bar{1}\bar{1}0)$  orientation, which were also obtained from the reconstructed three-dimensional momentum distribution. The spectrum shows a minimum at the center, consistent

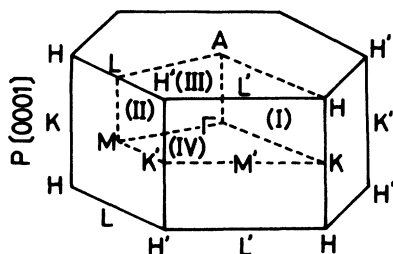


FIG. 1. First Brillouin zone of graphite.

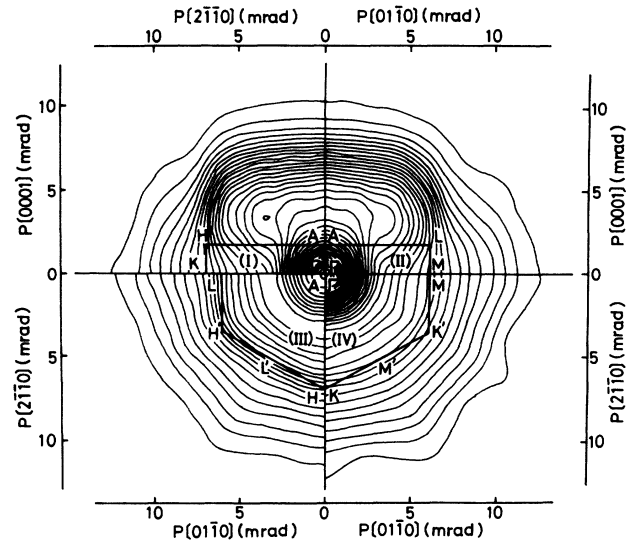


FIG. 2. Momentum-density contour maps of graphite of the cross sections (I)–(IV) of the Brillouin zone.

with the results obtained by 1D-ACAR (Refs. 8 and 9) and Doppler broadening.<sup>10</sup>

Contours are seen to be dense along  $\overline{LH}$  and  $\overline{HH'}$  of the cross section (III) shown in Fig. 2. Dense contours indicate a discontinuity in the momentum distribution, and in this case they coincide with the zone-edges of the first Brillouin zone,  $\overline{LH}$  and  $\overline{HH'}$ , calculated from the crystal symmetry of graphite. The notations shown on the maps correspond to those of the first Brillouin zone. On the cross sections (I) and (II), contours approach the  $\Gamma$  point in the region of lower  $p[0001]$ . This is explained in terms of the ground state  $\pi$ -electron wave function, which is symmetrical with respect to the graphite plane. The contours are heavily concentrated around the  $\Gamma$  point of the cross sections (I), (II), and (IV). These concentrated contours are ascribed to the superposition of the momentum densities in positronium (PS) and the graphite bulk. Figure 2, cross section (IV) shows a two-dimensional momentum distribution of the cross section at  $p[0001]=0$ . The distribution is found to be isotropic

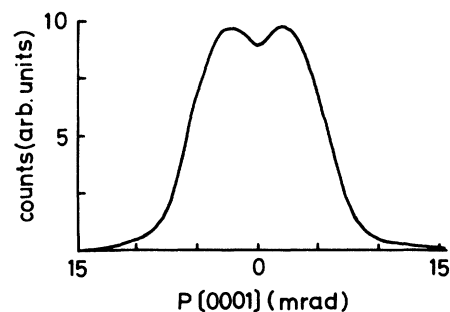


FIG. 3. Positron-electron annihilation counts integrated along the  $p[01\bar{1}0]$  of the 2D-ACAR spectrum for the  $(2\bar{1}\bar{1}0)$  orientation.

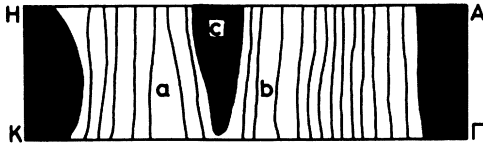


FIG. 4. LCW rate contour map of the cross section (I) of the first Brillouin zone of graphite.

in the region of less than 3 mrad, and the contours are denser in the central region of 0–2 mrad than those in the higher-momentum region.

Figures 4–7 show contour maps of the LCW rate obtained through periodic superposition of the momentum densities of the cross sections (I)–(IV) shown in Fig. 2. An extremely high LCW rate is found to be distributed cylindrically around the  $A$ - $\Gamma$  line, but it decreases sharply out to a radius of  $\sim 0.4\overline{\Gamma K}$ . This cylindrical distribution of momentum density is ascribed to Ps located on inner surfaces of the graphite, as found in slow-positron annihilation studies.<sup>11</sup>

Figure 4 shows hollows ( $a$ ) and ( $b$ ), and a ridge ( $c$ ), in the LCW rate at distances of  $\sim 0.65\overline{\Gamma K}$ ,  $0.45\overline{\Gamma K}$ , and  $0.57\overline{\Gamma K}$  from the  $A$ - $\Gamma$  line, respectively. The LCW rate in this region increases from the hollow ( $b$ ) to the zone edge  $H\overline{K}$ , and the rates at the ridge ( $c$ ) and the edge are, respectively, 1.04 and 1.05 times higher than the rate at the hollow ( $a$ ). The LCW-rate contour map corresponding to the momentum density of the cross section (II) shows a hollow ( $d$ ) at a distance of  $\sim 0.77\overline{\Gamma M}$  from the  $\Gamma$  point and a projection ( $e$ ) at a distance of  $\sim 0.65\overline{AL}$  from the  $A$  point (Fig. 5). The LCW rate increases from the hollow ( $d$ ) to the zone edge  $L\overline{M}$ , and the rates at the projection ( $e$ ) and the zone edge are 1.04 and 1.05 times higher than the rate at the hollow ( $d$ ). The hollows ( $a$ ), ( $b$ ), and ( $d$ ); and the projections ( $c$ ) and ( $e$ ) shown in Figs. 6 and 7 correspond, respectively, to the hollows ( $a$ ), ( $b$ ), and ( $d$ ); the ridge ( $c$ ); and the projection ( $e$ ) shown in Figs. 4 and 5.

In order to compare our experimental results with theoretical ones, we reproduce theoretically obtained LCW-rate contour maps from Ref. 4, as shown in Fig. 8. They were obtained from a numerical basis-set linear combination of atomic orbitals  $X\alpha$  band calculation. Figure 8(a) shows a ridge at a distance of  $\sim 0.57\overline{\Gamma K}$  from the  $A$ - $\Gamma$  line. The appearance of this ridge has been explained in terms of a contribution from a  $\sigma$  band. The experimentally determined ridge ( $c$ ) in Fig. 4 is located at

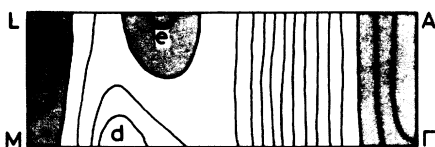


FIG. 5. LCW-rate contour map of the cross section (II) of the first Brillouin zone of graphite.

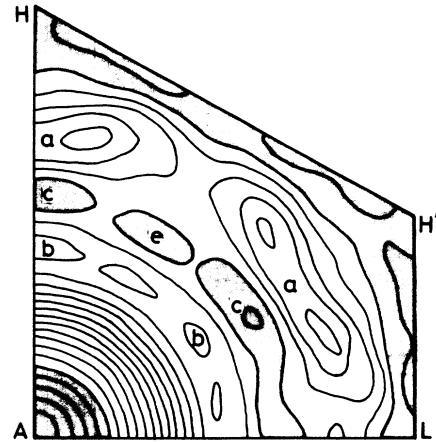


FIG. 6. LCW-rate contour map of the cross section (III) of the first Brillouin zone of graphite.

the same position as the theoretically predicted one, and so is attributed to the  $\sigma$  band.

In Fig. 8, the LCW rate due to the  $\pi$  band increases, while the rate due to the  $\sigma$  band decreases around the zone edge. The experimentally determined LCW rate increases around the zone edge, as shown in Figs. 4 and 5, and so is ascribed to a dominant  $\pi$ -band contribution.

The calculated LCW rate due to the  $\pi$ -band shows a hollow at a distance of  $\sim 0.65\overline{\Gamma M}$  from the  $\Gamma$  point, and a projection at a distance of  $\sim 0.56\overline{AL}$  from the  $A$  point, as shown in Fig. 8(b). The ratio of the rate at the projection to that at the hollow is estimated at  $\sim 4.2$ . This figure is larger than the experimental ratio observed for the projection ( $e$ ) and the hollow ( $d$ ), shown in Fig. 5. The calculated LCW rate due to the  $\sigma$  band shows a projection and a hollow at the positrons where the calculated rate due to the  $\pi$  band shows a hollow and a projection, respectively, so that the combined rates at these positrons

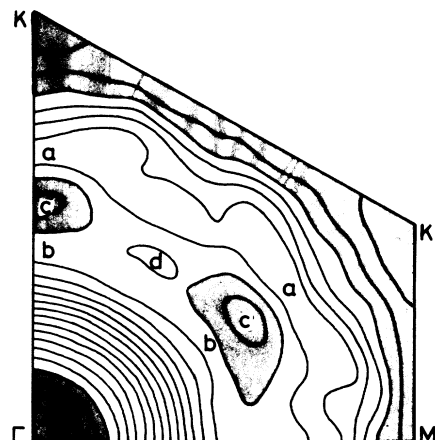


FIG. 7. LCW-rate contour map of the cross section (IV) of the first Brillouin zone of graphite.

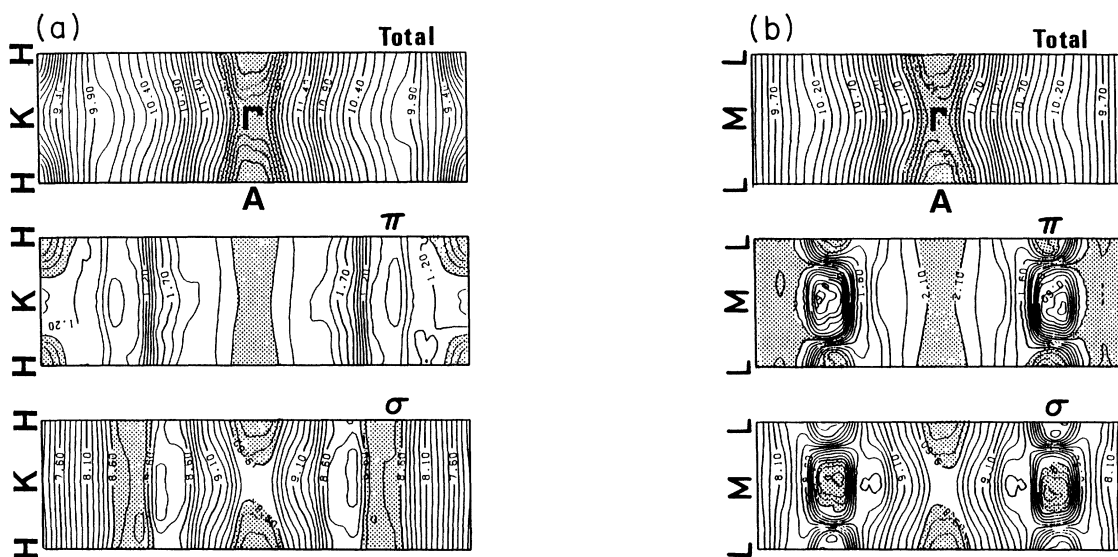


FIG. 8. Theoretical contour maps of the LCW rate as a function of  $k$  points on (a) the  $\Gamma$ - $K$  plane and (b) the  $\Gamma$ - $M$  plane, reproduced from Ref. 4. Total LCW rate and  $\pi$ - and  $\sigma$ -band contributions are plotted.

are expected to be featureless. However, the experimentally determined map shows a hollow ( $d$ ) and a projection ( $e$ ) in the regions where the calculated rate due to the  $\pi$  band predicts a hollow and a projection. This demonstrates a greater contribution from the  $\pi$  band than from the  $\sigma$  band.

The ratio of the contribution from the  $\pi$  band to that from the  $\sigma$  band is theoretically estimated at  $1/6$  in Ref. 4, smaller than the value obtained by Berko *et al.*<sup>8</sup> and Colombino *et al.*<sup>9</sup> The experimental LCW-rate map is compared with the maps calculated on the basis of various combinations of the theoretical  $\pi$ - and  $\sigma$ -band contributions given in Ref. 4, but any map does not agree satisfactorily with the experimental one over the entire region. It only shows qualitative features of the experimental result. This may be due to the fact that  $1s$ ,  $2s$ , and  $2p$  atomic wave functions were adopted as basis functions for the positron in the calculation. The positron is

known, however, not to be localized within layers in graphite, but to spread into the interlayer region.<sup>12</sup> Agreement may be improved if nonatomic functions are used for the positron, and another type of positron-electron correlation is considered in simulation.

#### ACKNOWLEDGMENTS

The authors wish to express their sincere thanks to the authors of Ref. 4 and Elsevier Sequoia S.A. for permission to reproduce the figure from Ref. 4. They also express their gratitude to Professor S. Tanuma and Professor H. Suematsu for a gift of purified Kish graphite and to Professor S. Berko, Professor K. G. Lynn, Professor H. Murakami, Professor T. Enoki, Professor R. Saito, Professor P. Sferlazzo, and Professor A. Ishii for valuable discussions.

\*Present address: Electrotechnical Laboratory, Tsukuba 305, Japan.

<sup>1</sup>R. N. West, *Adv. Phys.* **22**, 263 (1973).

<sup>2</sup>I. Kanazawa, S. Tanigawa, R. Suzuki, Y. Mizuhara, M. Sano, and H. Inokuchi, *J. Phys. Chem. Solids* **48**, 701 (1987).

<sup>3</sup>D. G. Lock, V. H. Crisp, and R. N. West, *J. Phys. F* **3**, 561 (1973).

<sup>4</sup>R. Saito, N. Shima, and H. Kamimura, *Synth. Met.* **23**, 217 (1988).

<sup>5</sup>S. Berko, in *Proceeding of the International School of Physics "Enrico Fermi,"* Course LXXXIII, edited by W. Brandt and A. Dupasquier (North-Holland, New York, 1983), p. 64.

<sup>6</sup>F. Sinclair, W. S. Farmer, and S. Berko, in *Positron Annihilation*, edited by P. G. Coleman, S. C. Sharma, and L. M. Diana (North-Holland, New York, 1982), p. 319.

<sup>7</sup>S. Tanigawa, S. Terakado, K. Ito, A. Morisue, and N. Shiotani, in *Positron Annihilation*, edited by P. C. Jain, R. M. Singru, and K. P. Gopinathan (World Scientific, Singapore, 1985), p. 282.

<sup>8</sup>S. Berko, R. E. Kelley, and J. S. Plaskett, *Phys. Rev.* **106**, 824 (1957).

<sup>9</sup>P. Colombino, B. Fiscella, and L. Trossi, *Nuovo Cimento* **27**, 589 (1963).

<sup>10</sup>M. Shimotamai, T. Iwata, T. Takahashi, and M. Doyama, *J. Phys. Soc. Jpn.* **52**, 694 (1983).

<sup>11</sup>P. Sferlazzo, S. Berko, K. G. Lynn, A. P. Mills, Jr., L. O. Roelling, A. J. Viescas, and R. N. West, *Phys. Rev. Lett.* **60**, 538 (1988).

<sup>12</sup>M. Sano, I. Kanazawa, H. Murakami, Y. Sakurai, T. Enoki, and H. Inokuchi, *Chem. Phys. Lett.* **122**, 143 (1985).

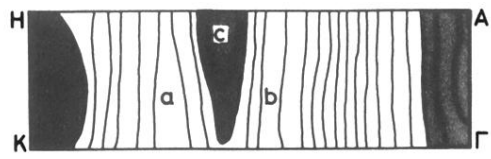


FIG. 4. LCW rate contour map of the cross section (I) of the first Brillouin zone of graphite.

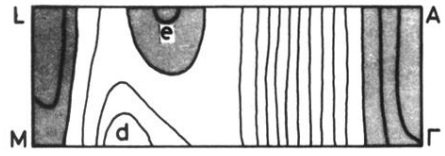


FIG. 5. LCW-rate contour map of the cross section (II) of the first Brillouin zone of graphite.

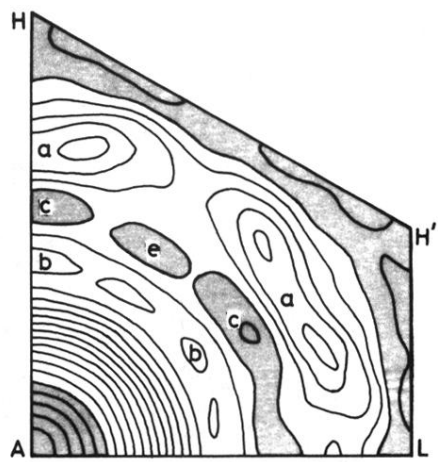


FIG. 6. LCW-rate contour map of the cross section (III) of the first Brillouin zone of graphite.

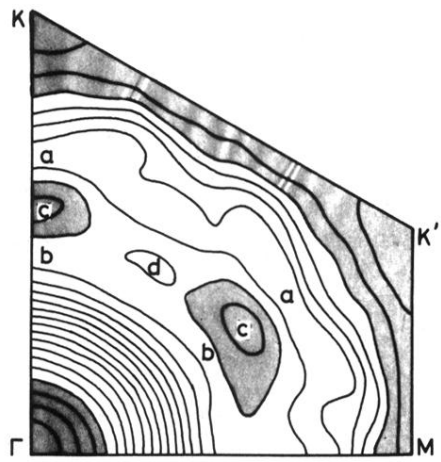


FIG. 7. LCW-rate contour map of the cross section (IV) of the first Brillouin zone of graphite.

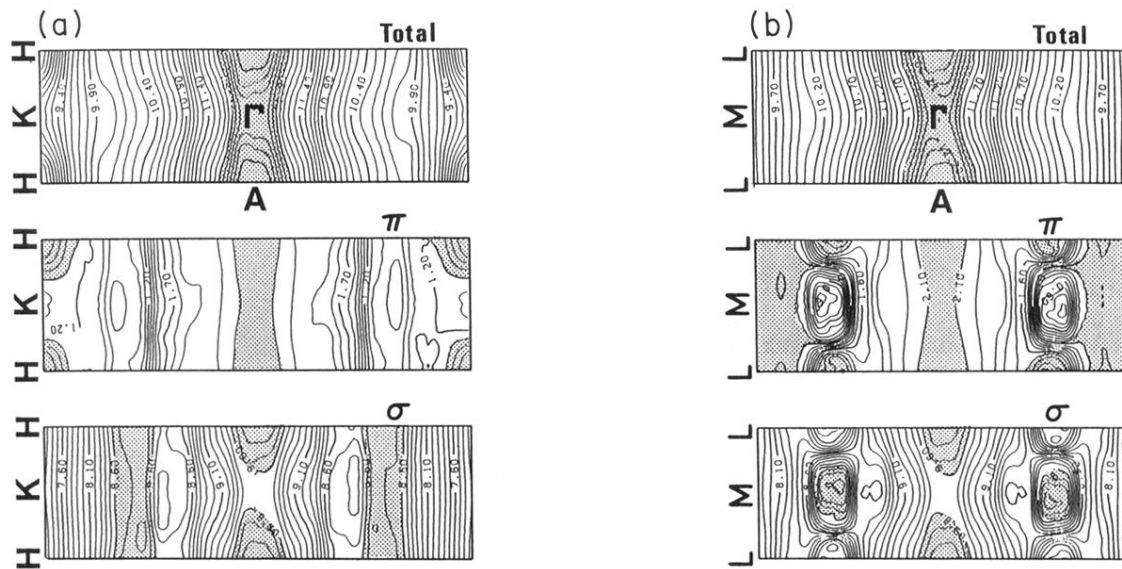


FIG. 8. Theoretical contour maps of the LCW rate as a function of  $k$  points on (a) the  $\Gamma$ - $K$  plane and (b) the  $\Gamma$ - $M$  plane, reproduced from Ref. 4. Total LCW rate and  $\pi$ - and  $\sigma$ -band contributions are plotted.